

Strain, magnetic anisotropy, and anisotropic magnetoresistance in (Ga,Mn)As on high-index substrates: Application to (113)A-oriented layers

L. Dreher,* D. Donhauser, J. Daeubler, M. Glunk, C. Rapp, W. Schoch, R. Sauer, and W. Limmer
Institut für Halbleiterphysik, Universität Ulm, 89069 Ulm, Germany

(Received 15 February 2010; revised manuscript received 11 May 2010; published 7 June 2010)

Based on a detailed theoretical examination of the lattice distortion in high-index epilayers in terms of continuum mechanics, expressions are deduced that allow the calculation and experimental determination of the strain tensor for (*hhl*)-oriented (Ga,Mn)As layers. Analytical expressions are derived for the strain-dependent free-energy density and for the resistivity tensor for monoclinic and orthorhombic crystal symmetries, phenomenologically describing the magnetic anisotropy and anisotropic magnetoresistance by appropriate anisotropy and resistivity parameters, respectively. Applying the results to (113)A orientation with monoclinic crystal symmetry, the expressions are used to determine the strain tensor and the shear angle of a series of (113)A-oriented (Ga,Mn)As layers by high-resolution x-ray diffraction and to probe the magnetic anisotropy and anisotropic magnetoresistance at 4.2 K by means of angle-dependent magnetotransport. Whereas the transverse-resistivity parameters are nearly unaffected by the magnetic field, the parameters describing the longitudinal resistivity are strongly field dependent.

DOI: [10.1103/PhysRevB.81.245202](https://doi.org/10.1103/PhysRevB.81.245202)

PACS number(s): 75.50.Pp, 75.47.-m, 75.30.Gw

I. INTRODUCTION

For the past two decades, dilute magnetic semiconductors, and in particular ferromagnetic semiconductors, have been attracting considerable attention due to their exceptional physical properties as well as their potential applicability in information technology. Ferromagnetism mediated by delocalized *p*-type carriers¹ could be implemented in the standard semiconductor GaAs by incorporating magnetic Mn atoms on Ga sites, cf. Ref. 2 and references therein. Since the highest Curie temperature reported so far is 185 K,³ the application of (Ga,Mn)As in electronic devices operating at room temperature seems to be doubtful. Nevertheless, due to its specific electronic and magnetic properties, (Ga,Mn)As represents an ideal test system for future spintronic applications.

Magnetic anisotropy (MA) and anisotropic magnetoresistance (AMR) are well established key features of (Ga,Mn)As, largely arising from spin-orbit coupling in the valence band. Consequently, both MA and AMR strongly depend on crystal symmetry and strain.^{1,4–8} On the one hand, this dependence defines the magnetic hard and easy axes,^{2,4,9} controlling the orientation of the magnetization and thus the electrical resistivity. On the other hand, it offers a method to intentionally manipulate the magnetic properties, e.g., by applying external strain via piezoelectric actuators^{6,9–12} or by lithographically induced strain relaxation.^{6,13,14} In any case, a quantitative description of the relation between crystal structure and MA and AMR, ideally by means of analytical expressions, is imperative.

So far, most of the published work focuses on (Ga,Mn)As grown on (001)-oriented substrates while only few publications report on (Ga,Mn)As grown on high-index substrates such as (113) and (114),^{15–19} where the description of the MA and the AMR is more complicated due to the reduced crystal symmetry. Potential applications of high-index (Ga,Mn)As are ridge structures with (113)A sidewalls and (001) top layers,²⁰ which could be used, e.g., for memory devices exploiting different coercitive fields of the sidewalls

and top layers. Yet, a coherent theoretical description of the MA and AMR for layers on high-index substrates, which takes into account the symmetry of the strain tensor $\bar{\epsilon}$, is still missing.

In this work, we present a concise phenomenological description of the MA and AMR for (*hhl*)-oriented ferromagnetic layers. To this end, we describe the structural properties of epitaxial high-index layers in terms of continuum mechanics and apply the theoretical results to the case of (113)A orientation. High-resolution x-ray diffraction (HRXRD) measurements were performed on a series of (113)A-oriented (Ga,Mn)As layers to quantitatively determine the epitaxial strain and symmetry of the layers. The MA and AMR were investigated by angle-dependent magnetotransport measurements. In agreement with previous studies on (113)A-oriented (Ga,Mn)As,^{17–19} we observe a uniaxial MA along the [001] direction, which can now be explained in the light of our theoretical model. Whereas the transverse-resistivity parameters turn out to be nearly constant, a systematic dependence of the longitudinal-resistivity parameters on the strength of the external magnetic field is found.

The paper is organized as follows: in Sec. II A, we calculate the strain tensor $\bar{\epsilon}$ for (*hhl*)-oriented layers and provide formulas that allow experimental access to $\bar{\epsilon}$. The results are applied to (113)-oriented (Ga,Mn)As samples where the Bravais lattice is base-centered monoclinic. An extension of the theory to partially relaxed layers is given in Appendix A. In Sec. II B, we present a phenomenological expression for the MA taking into account the specific form of the strain tensor for (*hhl*)-oriented layers. In Sec. II C, we derive expressions for the longitudinal and transverse resistivities ρ_{long} and ρ_{trans} , respectively, which apply to monoclinic crystal symmetry and current direction along $[3\bar{3}2]$. The resistivity tensors for monoclinic and orthorhombic symmetries can be found in Appendix B. They are required in the derivation of ρ_{long} and ρ_{trans} for arbitrary current directions. In Secs. III A and III B, the experimental results of the HRXRD and magnetotransport studies are presented.

II. THEORETICAL CONSIDERATIONS

Crystal symmetry and epitaxial strain strongly influence the MA and the AMR. Therefore, we start with a detailed theoretical examination of the lattice distortion of (hkl) layers in terms of continuum mechanics and apply the general results to (113) -oriented layers (Sec. II A). Based on these results, we present phenomenological expressions for the MA in strained high-index ferromagnetic layers (Sec. II B). We present the resistivity tensors for monoclinic and orthorhombic symmetries (Appendix B) and calculate ρ_{long} and ρ_{trans} for monoclinic symmetry and current direction along $[3\bar{3}2]$ (Sec. II C).

A. Structural properties

1. Distortion of arbitrarily oriented epitaxial layers

The strain in an epitaxial layer can unambiguously be described by the distortion tensor \bar{A} with components $A_{ij} = du_i/dx_j$, where \mathbf{u} is the mechanical displacement field and x_i denote Cartesian coordinates along the cubic axes. In order to calculate the distortion of epitaxial layers grown on arbitrarily oriented cubic substrates, we decompose \bar{A} according to Hornstra and Bartels²¹

$$\bar{A} = \mathbb{1}\varepsilon_h + \mathbf{a} \otimes \mathbf{n}, \quad (1)$$

where \otimes denotes the dyadic product and

$$\varepsilon_h = \frac{a_s - a_l}{a_l} \quad (2)$$

is the isotropic strain that compresses (expands) the cubic unit cell of the layer to the size of the substrate's unit cell; a_s and a_l denote the lattice parameters of substrate and relaxed layer, respectively. \mathbf{n} is the unit vector perpendicular to the interface and \mathbf{a} is a vector that represents the anisotropic distortion of the layer. Figure 1 illustrates the superposition of the displacements described by Eq. (1): if we consider any mathematical point in the unstrained layer at the distance x from the interface, then this point has the distance $(1 + \varepsilon_h)x$ from the interface after applying $\mathbb{1}\varepsilon_h$. The displacement from this position into its final position is given by $\mathbf{a}\mathbf{x}$.

If the layer is in static equilibrium, there is no stress perpendicular to the surface. Applying Hooke's law, this constraint leads to the set of linear equations ($i=x, y, z$)

$$C_{ijkl}\varepsilon_k n_j = \sum_{jkl} \left[\varepsilon_h \delta_{kl} + \frac{1}{2}(a_k n_l + a_l n_k) \right] C_{ijkl} n_j = 0, \quad (3)$$

where

$$\varepsilon_{kl} = \frac{A_{kl} + A_{lk}}{2} \quad (4)$$

are the components of the (symmetrized) strain tensor and C_{ijkl} denote the elastic stiffness constants of the crystal. With given C_{ijkl} and \mathbf{n} , Eq. (3) can be solved for the components a_i , which are proportional to ε_h . Considering Eq. (1), the

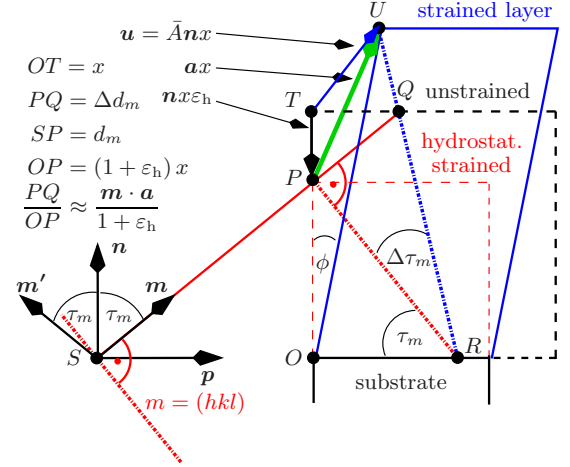


FIG. 1. (Color online) The points S , O , and R are located within the interface between substrate and layer. \mathbf{n} , \mathbf{p} , \mathbf{m} , and \mathbf{m}' are unit vectors. \mathbf{n} and \mathbf{p} are normal and parallel to the interface, respectively; \mathbf{m} and \mathbf{m}' are perpendicular to the lattice plane $m=(hkl)$ and $m'=(h'k'l')$. They lie within the plane spanned by \mathbf{n} and \mathbf{p} and are symmetrically oriented with respect to \mathbf{n} ($\tau_m = \tau_{m'}$). Before any strain is being applied, the point T has the distance x from the interface. The displacement to its final position U can be described as a superposition of a hydrostatic compression of the (unstrained) layer ($T \rightarrow P$) and a displacement by $\mathbf{a}\mathbf{x}$ ($P \rightarrow U$), cf. Eq. (1). The hydrostatically compressed layer has the same lattice plane spacing as the substrate and therefore Eqs. (5) and (6) can be derived considering only the displacement described by \mathbf{a} .

distortion tensor \bar{A} is then known as a linear function of the only remaining parameter ε_h , which can be determined experimentally as follows.

We label lattice planes by a single index m which stands for a Miller index triplet, e.g., $m=(hkl)$, and we sometimes refer to planes by their normal \mathbf{m} . A lattice plane m within a distorted layer in general encloses an angle $\Delta\tau_m$ with the corresponding lattice plane in the substrate, cf. Fig. 1. Furthermore, the distortion causes a relative difference $(\Delta d/d)_m$ between the lattice plane spacings in layer and substrate. Both, $(\Delta d/d)_m$ and $\Delta\tau_m$, are accessible via HRXRD and are related to ε_h by the expressions²¹

$$\left(\frac{\Delta d}{d} \right)_m = \frac{d_m^l - d_m^s}{d_m^s} = \frac{\mathbf{m} \cdot \mathbf{a}(\varepsilon_h)}{1 + \varepsilon_h} \cos \tau_m, \quad (5)$$

$$\Delta\tau_m = \frac{\mathbf{m} \cdot \mathbf{a}(\varepsilon_h)}{1 + \varepsilon_h} \sin \tau_m, \quad (6)$$

where τ_m is the angle between the surface normal and the lattice plane m . As described in detail in Ref. 22, the separation of layer and substrate peak decreases with decreasing layer thickness. Therefore, care has to be taken when determining $\Delta d/d$ and $\Delta\tau$ within the framework of kinematic x-ray theory.²² To give an example, for (001) -oriented $(\text{Ga,Mn})\text{As}$ layers with a manganese concentration of 5%, corresponding to a lattice mismatch $\Delta a/a \approx 0.21\%$,⁴ the peak

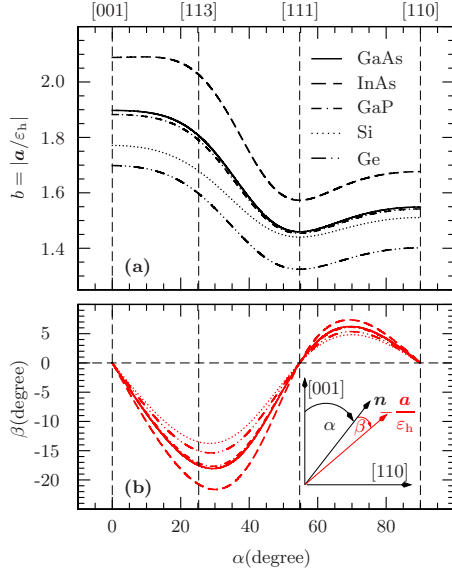


FIG. 2. (Color online) (a) Magnitude $b=|a/\varepsilon_h|$ and (b) angle β , calculated with various stiffness constants (Ref. 23), are plotted as a function of the angle α between \mathbf{n} and [001]. Only for the highly symmetric crystal orientations [001], [111], and [110] \mathbf{a} aligns with \mathbf{n} .

shift exceeds 2% if the layer thickness is smaller than 100 nm, cf. Eq. (4) in Ref. 22.

In the remainder of the paper, we focus on the practically relevant case of (hhl) -oriented substrates. Solving Eq. (3) for substrate orientations \mathbf{n} between [001] and [110], the vector \mathbf{a} reads as

$$\mathbf{a} = -b \begin{pmatrix} \sin(\alpha + \beta)/\sqrt{2} \\ \sin(\alpha + \beta)/\sqrt{2} \\ \cos(\alpha + \beta) \end{pmatrix} \varepsilon_h, \quad (7)$$

where b denotes the magnitude of the vector $-\mathbf{a}/\varepsilon_h$ and β the angle between \mathbf{n} and $-\mathbf{a}/\varepsilon_h$. In Fig. 2, b and β are plotted for several cubic semiconductors as a function of the angle α between \mathbf{n} and [001], using the elastic constants given in Ref. 23. The vector \mathbf{a} always lies within the $(1\bar{1}0)$ plane; thus, this plane is a symmetry element (mirror plane) for all layers grown on (hhl) substrates. Employing Eqs. (1), (4), and (7), the components of $\bar{\varepsilon}$ can be inferred from Fig. 2 using the equations

$$\varepsilon_{xx} = \varepsilon_{yy} = \varepsilon_h \left[1 - \frac{b}{2} \sin(\alpha + \beta) \sin \alpha \right], \quad (8)$$

$$\varepsilon_{zz} = \varepsilon_h [1 - b \cos(\alpha + \beta) \cos \alpha], \quad (9)$$

$$\varepsilon_{xy} = \varepsilon_{xx} - \varepsilon_h, \quad (10)$$

$$\varepsilon_{xz} = \varepsilon_{yz} = -\frac{b\varepsilon_h}{2\sqrt{2}} [\sin(\alpha + \beta) \cos \alpha + \cos(\alpha + \beta) \sin \alpha]. \quad (11)$$

Equations (8)–(11) are essential for the understanding of the MA and will be used in the derivation of the free-energy density in Sec. II B.

Figure 2 shows that for crystal facets other than (001), (110), and (111), \mathbf{a} is not aligned with the surface normal \mathbf{n} and the layer is therefore sheared toward a direction given by the projection of \mathbf{a} onto the surface (cf. Fig. 1). Employing Eq. (6), the shear angle ϕ of a \mathbf{n} -oriented layer toward any direction $\mathbf{p} \perp \mathbf{n}$, i.e., $\tau_p = 90^\circ$ is obtained from

$$\phi = \Delta\tau_p = \frac{\mathbf{p} \cdot \mathbf{a}(\varepsilon_h)}{1 + \varepsilon_h}, \quad (12)$$

where ε_h has to be determined by the procedure described above. ϕ can also be measured directly without making use of the stiffness constants and the explicit form of $\mathbf{a}(\varepsilon_h)$, if we choose two lattice planes m and m' with $\mathbf{p} = (\mathbf{m} - \mathbf{m}')/2 \sin \tau_m$; insertion into Eq. (12) yields

$$\phi = \frac{\mathbf{a}(\mathbf{m} - \mathbf{m}')}{2 \sin \tau_m (1 + \varepsilon_h)} \underset{\text{Eq. (6)}}{=} \frac{\Delta\tau_m - \Delta\tau_{m'}}{2 \sin^2 \tau_m}, \quad (13)$$

in agreement with Ref. 24. The angles $\Delta\tau_m$ and $\Delta\tau_{m'}$ can be derived from rocking curves as described in Sec. III A. Equation (13) is valid if the two lattice planes m and m' are equally inclined toward the surface, i.e., if $\tau_m = \tau_{m'}$, cf. Fig. 1.

So far, we have restricted our considerations to pseudo-morphologically grown layers. With minor modifications, Eqs. (5) and (6) can also be applied to partially relaxed layers. In Appendix A, we discuss how the relaxed lattice constant and the degree of relaxation can be inferred from reciprocal space maps (RSMs) for arbitrarily oriented substrates applying the formalism described above.

2. Application to (113)-oriented (Ga,Mn)As layers

We now apply the general equations derived in the preceding section to the case of (113)-oriented layers. For the following calculations, we use the elastic stiffness constants of GaAs given in Ref. 23 neglecting the Mn alloying. This assumption will be justified for (Ga,Mn)As layers with Mn concentrations below 5% by the experimental results presented in Sec. III A. From Fig. 2 we obtain for $\alpha = 25.2^\circ$ the values $b = 1.81$ and $\beta = -17.5^\circ$. Equation (7) then yields

$$\mathbf{a} = -1.81 \begin{pmatrix} 0.095 \\ 0.095 \\ 0.991 \end{pmatrix} \varepsilon_h. \quad (14)$$

With Eqs. (8)–(11) we find for the strain tensor

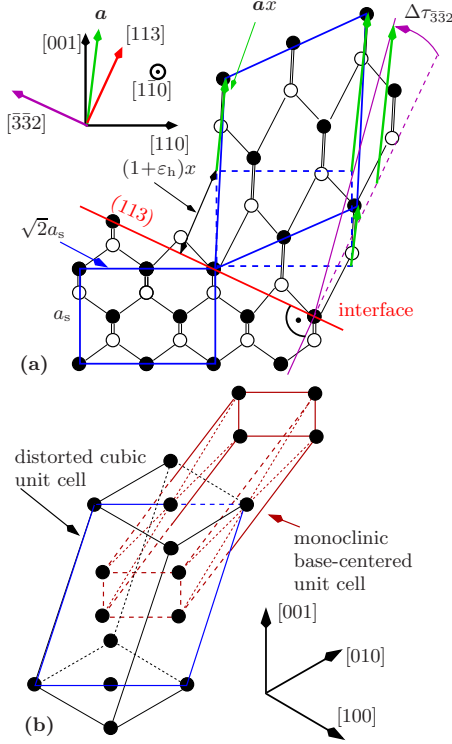


FIG. 3. (Color online) (Ga,Mn)As(113)A layers exhibit a monoclinic crystal symmetry. (a) The layer as a whole is sheared toward $[\bar{3}\bar{3}2]$ by an angle $\phi = \Delta\tau_{\bar{3}\bar{3}2}$, leaving the $(1\bar{1}0)$ mirror plane as the only remaining symmetry element. (b) Three-dimensional view of the monoclinic base-centered unit cell with respect to the distorted cubic unit cell. For the sake of clarity, the second basis atom of the zinc-blende lattice is omitted in this sketch.

$$\bar{\varepsilon} = \varepsilon_h \begin{pmatrix} +0.95 & -0.05 & -0.35 \\ -0.05 & +0.95 & -0.35 \\ -0.35 & -0.35 & -0.62 \end{pmatrix}. \quad (15)$$

Figure 3 schematically illustrates the crystal structure of the distorted (113) layer. The position of each atom in the strained layer was constructed by applying Eq. (1) together with Eq. (14): we start by putting a hydrostatically compressed layer on the substrate. The unit cell of the layer in this hypothetical state is identical to the unit cell of the substrate, cf. the dashed and solid cubic unit cells in Fig. 3(a). The final position of each atom can be found by a displacement along the direction given by \mathbf{a} , where the magnitude of the displacement is proportional to the distance x of the atom from the interface (cf. Fig. 1).

The distortion breaks the symmetry of the layer and the only remaining symmetry element is a $(1\bar{1}0)$ mirror plane; hence, the distorted crystal is assigned to the point group $m(C_s)$. This assignment is important for the derivation of the resistivity tensor presented in Appendix B. For clearness, the crystallographic unit cell of the distorted layer is depicted in Fig. 3(b); it becomes evident that the corresponding Bravais lattice is base-centered monoclinic.

In order to connect ε_h with the experimentally accessible quantity $(\Delta d/d)_m$, we apply Eq. (5) to the case of the sym-

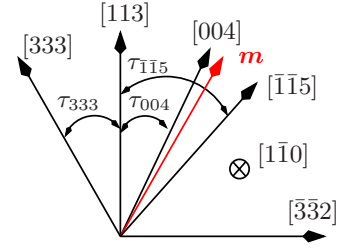


FIG. 4. (Color online) Normal vectors of the lattice planes considered in Eq. (18). Referring to Fig. 1, we chose $\mathbf{m}' = [333]$ and $\mathbf{p} = [\bar{3}\bar{3}2]$. We find a virtual lattice plane m with equal inclination with respect to the (113) plane by interpolation between the (004) and $(\bar{1}\bar{1}5)$ plane. For the corresponding angles we find $\tau_m = \tau_{333} = \tau_{004} + 0.27(\tau_{004} - \tau_{\bar{1}\bar{1}5})$.

metric $m = (113)$ reflection ($\tau_{113} = 0^\circ$), i.e., we consider lattice planes parallel to the surface. Equation (5) simplifies to

$$\left(\frac{\Delta d}{d}\right)_{113} = -1.723 \frac{\varepsilon_h}{1 + \varepsilon_h} = 1.723 \frac{a_1 - a_s}{a_s}. \quad (16)$$

With ε_h as obtained from Eq. (16), the shear angle of the (113) layer toward $[\bar{3}\bar{3}2]$ is inferred from Eq. (12), reading now as

$$\phi = \Delta\tau_{\bar{3}\bar{3}2} = -0.544 \frac{\varepsilon_h}{1 + \varepsilon_h} = 0.544 \frac{a_1 - a_s}{a_s}. \quad (17)$$

Figure 3(a) tells us that this shear angle ϕ of the layer as a whole is the same as the angle $\Delta\tau_{\bar{3}\bar{3}2}$ between the $(\bar{3}\bar{3}2)$ lattice planes of substrate and layer, respectively.

For a direct measurement of ϕ , we use Eq. (13). Referring to Figs. 1 and 4, we choose $\mathbf{m}' = [333]$ and find the corresponding plane m with equal inclination with respect to the (113) plane by interpolating between the $(\bar{1}\bar{1}5)$ plane and the (004) plane as described in Ref. 24. We obtain for the shear angle

$$\phi = \frac{\Delta\tau_{004} + 0.27(\Delta\tau_{004} - \Delta\tau_{\bar{1}\bar{1}5}) - \Delta\tau_{333}}{2 \sin^2(\tau_{333})}. \quad (18)$$

B. Magnetic anisotropy

MA is the dependence of a system's free-energy density F on the orientation of the magnetization direction $\mathbf{m} = \mathbf{M}/M$. In the following, we assume the sample to consist of a single ferromagnetic domain with a uniform magnetization whose magnitude M is assumed to be constant; we therefore analyze the quantity $F_M = F/M$.

For a phenomenological description of the MA in (hhl) -oriented (Ga,Mn)As layers, we expand F_M in powers of the components m_x , m_y , and m_z of \mathbf{m} along the cubic axes $[100]$, $[010]$, and $[001]$, respectively. Considering terms up to the fourth order in \mathbf{m} , the only intrinsic contribution to F_M for an undistorted cubic layer is a cubic anisotropy

$$F_M^{\text{cub.}} = B_{\text{cub.}}(m_x^4 + m_y^4 + m_z^4), \quad (19)$$

due to the crystal symmetry. Extrinsic contributions to F_M are the shape anisotropy, caused by the demagnetization field

perpendicular to the layer, and a uniaxial in-plane contribution, whose microscopic origin is under debate.^{5,25–28} Most likely the latter contribution originates from the incorporation of Mn which breaks the cubic symmetry of the lattice,⁵

$$F_M^{\text{ex}} = B_d(\mathbf{m} \cdot \mathbf{n})^2 + B_u(\mathbf{m} \cdot \mathbf{t})^2. \quad (20)$$

Here \mathbf{n} and \mathbf{t} denote unit vectors along the surface normal and $[\bar{1}10]$, respectively, and B_d is related to the magnetization M by $B_d = \mu_0 M/2$.

For distorted layers, further intrinsic contributions proportional to the strain components ε_{ij} occur. These are referred to as magnetoelastic contributions and are presented for arbitrarily strained cubic crystals in Ref. 29. Considering intrinsic and extrinsic contributions up to the fourth order in \mathbf{m} , the free-energy density for (hhl) -oriented layers can be written as

$$F_M(\mathbf{m}) = \text{const} + B_z m_z^2 + B_{xy} m_x m_y + B_{xz}(m_x + m_y) m_z + B_z^4 m_z^4 + B_{x^4}(m_x^4 + m_y^4) + B_{xyz^2} m_x m_y m_z^2 + B_{x^2 y z}(m_x + m_y) m_x m_y m_z + B_d(\mathbf{m} \cdot \mathbf{n})^2 + B_u(\mathbf{m} \cdot \mathbf{t})^2. \quad (21)$$

The anisotropy parameters are related to the strain components by

$$B_{z^2} = b_1(\varepsilon_{xx} - \varepsilon_{zz}), \quad (22)$$

$$B_{xy} = 2b_2 \varepsilon_{xy}, \quad (23)$$

$$B_{xz} = 2b_2 \varepsilon_{xz}, \quad (24)$$

$$B_{x^4} = b_4 \varepsilon_{xx} - \frac{3b_3 + 2b_4}{6}(2\varepsilon_{xx} + \varepsilon_{zz}) - \frac{B_{\text{cub}}}{2}, \quad (25)$$

$$B_{z^4} = b_4 \varepsilon_{zz} - \frac{3b_3 + 2b_4}{6}(2\varepsilon_{xx} + \varepsilon_{zz}) - \frac{B_{\text{cub}}}{2}, \quad (26)$$

$$B_{xyz^2} = 2b_5 \varepsilon_{xy}, \quad (27)$$

$$B_{x^2 z^2} = 2b_5 \varepsilon_{xz}. \quad (28)$$

The parameters b_i denote magnetoelastic coupling constants. Using the trivial identity $m_x^2 + m_y^2 + m_z^2 = 1$, the contribution $B_{xy} m_x m_y$ in Eq. (21) can be expressed in terms of $B_u(\mathbf{m} \cdot \mathbf{t})^2$ and $B_z m_z^2$. Therefore, we will understand it to be contained in the latter terms in the analysis of the experimental data in Sec. III B.

In the case of (001)-oriented layers, the off-diagonal elements of $\bar{\varepsilon}$ vanish and Eq. (21) simplifies to the well-known expression

$$F_M(\mathbf{m}) = \text{const} + (B_{z^2} + B_d) m_z^2 + B_z^4 m_z^4 + B_{x^4}(m_x^4 + m_y^4) + \frac{1}{2} B_u (m_x - m_y)^2. \quad (29)$$

Equation (21), in particular, explains in a natural way the occurrence of the uniaxial anisotropy $B_{z^2} m_z^2$ along $[001]$, which has been introduced *ad hoc* in previous publications

in order to explain the results of angle-dependent ferromagnetic resonance^{17,18} and magnetotransport studies^{18,19} on (113)A-oriented (Ga,Mn)As layers.

Furthermore, Eqs. (22), (25), and (26) account for the strain dependence of the parameters B_{z^2} , B_{x^4} , and B_{z^4} (Ref. 30) found in a systematic study of (Ga,Mn)As layers grown on relaxed (001)-oriented (In,Ga)As buffers:⁴ for (001) orientation, the relation $\varepsilon_{xx} \approx -1.1\varepsilon_{zz}$ holds and therefore Eqs. (25) and (26) read as $B_{x^4} = (0.6b_3 - 0.7b_4)\varepsilon_{zz} - B_{\text{cub}}/2$ and $B_{z^4} = (0.6b_3 + 1.4b_4)\varepsilon_{zz} - B_{\text{cub}}/2$, respectively. Figure 10 in Ref. 4 shows an increase in B_{x^4} and a decrease in B_{z^4} with increasing ε_{zz} . These findings agree with Eqs. (25) and (26) if $b_3 > 7b_4/6$ and $b_3, b_4 < 0$.

C. Anisotropic magnetoresistance

It is well established that (similar to the MA) the AMR, described by the resistivity tensor $\bar{\rho}(\mathbf{m})$, is strongly affected by the crystal symmetry. In order to obtain an analytical expression for $\bar{\rho}(\mathbf{m})$, we performed a symmetry-based series expansion of the tensor components up to the fourth order in \mathbf{m} . For cubic and tetragonal symmetries, the explicit form of the resistivity tensor and a detailed description of its derivation can be found in Ref. 31. In this work, we generalize the expressions for $\bar{\rho}(\mathbf{m})$ to monoclinic and orthorhombic symmetries. As shown in Fig. 10 of Appendix B, orthorhombic symmetry applies to (110)-oriented substrates. For other crystal facets (hhl) with $0 \neq h \neq l$, the crystal exhibits monoclinic symmetry. The explicit forms of the corresponding tensors $\bar{\rho}(\mathbf{m})$ are given in Appendix B.

The AMR is usually probed by measuring the longitudinal and transverse resistivities ρ_{long} and ρ_{trans} , respectively, which are related to $\bar{\rho}(\mathbf{m})$ by $\rho_{\text{long}} = \mathbf{j}^T \cdot \bar{\rho} \cdot \mathbf{j}$ and $\rho_{\text{trans}} = \mathbf{t}^T \cdot \bar{\rho} \cdot \mathbf{j}$. The unit vectors \mathbf{j} and \mathbf{t} point along the current direction and the transverse direction, respectively. The resistivities also allow experimental access to the MA as shown in Refs. 4, 18, and 31. In Sec. II B, the magnetic anisotropy parameters introduced in the preceding section are derived experimentally by measuring the angular dependence of ρ_{long} and ρ_{trans} at various fixed magnetic field strengths.

Now we turn to (113)-oriented layers. According to our previous work,³¹ we are referring to the right-handed coordinate system $(\mathbf{j}, \mathbf{t}, \mathbf{n})$, where $\mathbf{j} \parallel [33\bar{2}]$, $\mathbf{t} \parallel [\bar{1}10]$, and $\mathbf{n} \parallel [113]$; m_j , m_t , and m_n denote projections of \mathbf{m} along these directions. We calculate ρ_{long} and ρ_{trans} by projecting the resistivity tensor in Eqs. (B4) along \mathbf{j} and \mathbf{t} , respectively. We find

$$\rho_{\text{long}} = \rho_0 + \rho_1 m_j^2 + \rho_2 m_n^2 + \rho_3 m_j^4 + \rho_4 m_n^4 + \rho_5 m_j^2 m_n^2 + \rho_{01} m_j m_n + \rho_{02} m_j^3 m_n + \rho_{03} m_j m_n^3 \quad (30)$$

and

$$\rho_{\text{trans}} = \rho_6 m_n + \rho_7 m_j m_t + \rho_8 m_n^3 + \rho_9 m_j m_t m_n^2 + \rho_{10} m_j^3 m_t + \rho_{11} m_t m_n + \rho_{12} m_t m_n^3 + \rho_{13} m_j + \rho_{14} m_j^3 + \rho_{15} m_j^2 m_n + \rho_{16} m_j m_n^3 + \rho_{17} m_j^2 m_t m_n, \quad (31)$$

where ρ_i are linearly independent resistivity parameters related to the expansion coefficients of $\bar{\rho}$. In the limit of unstrained layers (cubic symmetry) the expressions for ρ_{long}

and ρ_{trans} have the same form as in Eqs. (30) and (31), however several resistivity parameters become linearly dependent. This is due to the fact that the current direction along $[3\bar{3}2]$ already breaks the cubic symmetry.

AMR studies frequently focus on the special case where the magnetization lies within the layer plane ($m_n=0$). Equations (30) and (31) then simplify to

$$\rho_{\text{long}} = \rho_0 + \rho_1 m_j^2 + \rho_3 m_j^4 \quad (32)$$

and

$$\rho_{\text{trans}} = \rho_7 m_j m_t + \rho_{10} m_j^3 m_t + \rho_{13} m_j + \rho_{14} m_j^3. \quad (33)$$

III. EXPERIMENT

We apply the theoretical expressions obtained in the preceding section to a series of (113)A(Ga,Mn)As layers with different Mn concentrations. In Sec. III A, the hydrostatic strain ε_h and thus $\bar{\varepsilon}$ as well as the shear angle of the layers are derived quantitatively from HRXRD measurements. In Sec. III A, we present angle-dependent magnetotransport measurements which are theoretically described by the expressions for ρ_{long} and ρ_{trans} given by Eqs. (30) and (31) and by the free-energy density given by Eq. (21).

A. HRXRD measurements

(Ga,Mn)As layers with manganese contents up to 5% were grown on (113)A-oriented GaAs substrates by low-temperature molecular-beam epitaxy as described in Refs. 32 and 33. The structural properties of the (Ga,Mn)As layers were experimentally investigated by HRXRD. We used a Bruker Siemens D5000HR x-ray diffractometer operating with the Cu K_{α_1} radiation ($\lambda=0.154$ nm). In order to measure the strain ε_h and the thickness of the (Ga,Mn)As(113)A layers, we performed ω - 2Θ scans from the symmetric (113) reflection. From the angular spacing of the layer thickness fringes,³⁴ we inferred a layer thickness of 150 nm. Employing Bragg's law, the ω - 2Θ scan yields $(\Delta d/d)_{113}$, and via Eq. (16) we obtained the hydrostatic strain ε_h . With that value of ε_h , we calculated the shear angle ϕ of the layer toward $[\bar{3}32]$ using Eq. (17). In Fig. 5, ε_h and ϕ are plotted against the Mn content.

In order to verify the consistence of the formalism presented in Sec. II A 1, we measured the shear angle ϕ of several samples directly by applying Eq. (18). We inferred the angles $\Delta\tau_{333}$, $\Delta\tau_{004}$, and $\Delta\tau_{\bar{1}\bar{1}5}$ from ω scans (rocking curves) with opened detector slits at high (+) and low (-) incidence. For an asymmetric reflection, as, e.g., the (333) reflection, the corresponding lattice plane encloses an angle τ_{333} with the surface and the reflex can be measured at two different angles $\omega_{333}^{\pm} = \Theta_{333} \pm \tau_{333}$ with respect to the surface, where Θ_{333} is the Bragg angle of the (333) reflection.³⁵ If the peak separation $\Delta\omega_{333}$ of layer and substrate is measured at high and low incidence, $\Delta\tau_{333}$ can be determined via $\Delta\tau_{333} = (\Delta\omega_{333}^+ - \Delta\omega_{333}^-)/2$. In Fig. 5, the results for the shear angle ϕ obtained in this manner are shown in comparison to those derived from the ω - 2Θ scans. The excellent agreement of the

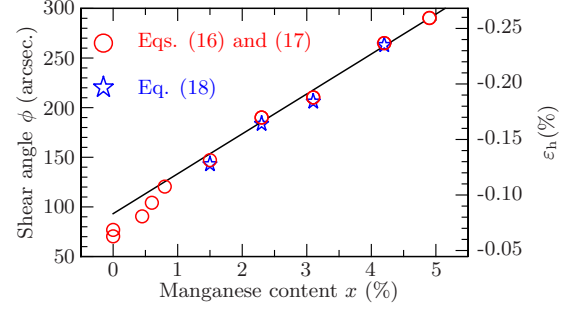


FIG. 5. (Color online) Shear angle ϕ toward the $[\bar{3}32]$ direction and hydrostatic strain ε_h of (113)A-oriented (Ga,Mn)As layers plotted as a function of the manganese concentration. The circles represent values for ε_h and ϕ derived from ω - 2Θ scans using Eqs. (16) and (17), respectively. The stars denote values for ϕ derived from rocking curves applying Eq. (18). Note that for the layer thickness $h=150$ nm the $\Delta d/d$ and $\Delta\tau$ values obtained from the peak separations cannot be considered reliable for Mn concentrations below approximately 2% (Ref. 22).

values confirms the consistency of the theoretical formalism. Furthermore, it demonstrates that the elastic stiffness constants of GaAs are a good approximation for those of (Ga,Mn)As within the investigated range of Mn concentrations.

B. Magnetotransport measurements

Most of the samples under study were found to be insulating at $T=4.2$ K and could therefore not be investigated by magnetotransport. The hole densities and Curie temperatures of the three conducting samples were determined from high-field magnetotransport measurements as described in Ref. 36. The results are summarized in Table I.

In order to investigate the MA and AMR in the (113)A-oriented (Ga,Mn)As samples, we performed angle-dependent magnetotransport measurements.^{4,18,31} For this purpose, the samples were patterned into 0.3-mm-wide Hall-bar structures oriented along $[3\bar{3}2]$ with Ohmic Au-Pt-Ti contacts and the longitudinal voltage probes separated by 1 mm. The dc density was 220 A cm⁻². The samples were mounted on a rotatable sample holder in a liquid-He-bath cryostat, which was placed between the poles of a Lake Shore electromagnet. With this setup, the magnetic field could be rotated arbitrarily with respect to the crystallographic axes of the (Ga,Mn)As layer.

We rotated the external field \mathbf{H} at various fixed field strengths within the three different crystallographic planes

TABLE I. Structural and electronic properties of metallic samples, studied via angle-dependent magnetotransport, cf. Sec. II B.

x_{Mn} (%)	ε_h (%)	P (10^{20} cm ⁻³)	T_C (K)
4.9	-0.26	2.0	44
4.2	-0.23	2.2	47
3.1	-0.18	2.1	38

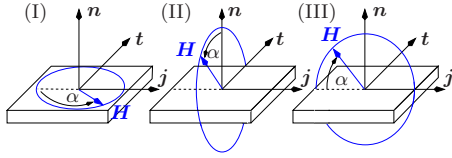


FIG. 6. (Color online) Configurations (I), (II), and (III) for angle-dependent magnetotransport measurements. The external magnetic field \mathbf{H} was rotated within the planes normal to $\mathbf{n} \parallel [113]$, $\mathbf{j} \parallel [332]$, and $\mathbf{t} \parallel [\bar{1}10]$.

depicted in Fig. 6 and measured ρ_{long} and ρ_{trans} . In the presence of an external magnetic field \mathbf{H} , the free-enthalpy density $G_M = G/M$ instead of the free-energy density F_M determines the magnetization orientation. We thus write

$$G_M(\mathbf{H}) = F_M(\mathbf{m}) - \mu_0 \mathbf{m} \cdot \mathbf{H} \quad (34)$$

with $F_M(\mathbf{m})$ from Eq. (21). The orientation \mathbf{m} of the magnetization at a given external field \mathbf{H} can be found by minimizing Eq. (34) with respect to \mathbf{m} . At the maximum applied field of $\mu_0 H = 0.62$ T, the Zeeman term $\mu_0 \mathbf{H} \mathbf{m}$ dominates the free-enthalpy density and \mathbf{m} essentially aligns along \mathbf{H} . With decreasing field strength however, the MA described by the anisotropy parameters in Eq. (21) more and more governs the motion of the magnetization as \mathbf{H} is rotated with respect to the sample.

By fitting Eqs. (30) and (31) to our experimental data recorded at $\mu_0 H = 0.62$ T, we obtained values for the resistivity parameters ρ_i . Using these parameters, we simulated the measured angular dependencies of ρ_{long} and ρ_{trans} at weaker fields by varying the anisotropy parameters until the simulated curves fit the experiment. Figure 7 exemplarily

shows the experimental and simulated angular dependencies of ρ_{long} and ρ_{trans} for the sample with 4.9% Mn.

The experimentally obtained anisotropy parameters are listed in Table II. In agreement with other work,^{18,19} the MA in our samples can be described by the parameters B_{x^4} , B_{z^4} , B_{z^2} , B_d , and B_u . As expected, the shape anisotropy parameter $B_d = \mu_0 M/2$ increases with increasing Mn concentration. Since both, the Mn concentration and the epitaxial strain, influence the parameters B_{x^4} , B_{z^4} , and B_{z^2} , it is not possible to infer an unambiguous strain dependence of these parameters from our experiment. Nevertheless, some qualitative conclusions can be drawn: because the relations $B_{x^4} - B_{z^4} = b_4(\varepsilon_{xx} - \varepsilon_{zz}) \approx 1.57b_4 \varepsilon_h > 0$ and $\varepsilon_h < 0$ hold for all samples, we find a negative magnetoelastic coupling parameter b_4 in agreement with the discussion in Sec. II B. Since the parameters B_{xz^2} , $B_{x^2z^2}$, and $B_{xy^2z^2}$ are negligible (the influence of B_{xy} is contained in B_{z^2} and B_u due to the linear dependence mentioned earlier), we are led to the conclusion that the coupling parameters b_2 and b_5 are smaller than b_1 (at least for the samples with $x_{\text{Mn}} > 4\%$). For more strongly strained samples or for samples with larger coupling parameters b_i , however, all anisotropy parameters given in Eqs. (22)–(27) may play a role. Recently, Zemen *et al.*⁵ published a theoretical survey on magnetocrystalline anisotropies in (Ga,Mn)As and compared their findings to available experimental data. The samples studied here exhibit the largest projection of the easy axis on the $[100]$ and $[010]$ axes, cf. (II). These findings are in agreement with the experimental data summarized in Ref. 5 for the given manganese concentrations, temperature, and hole concentration.

In contrast to our previous experiments,^{18,31} the drastic change in the longitudinal-resistivity curves, in particular, those obtained in configuration (I), upon variation in the external field strength (cf. Figs. 6 and 7) cannot solely be ex-

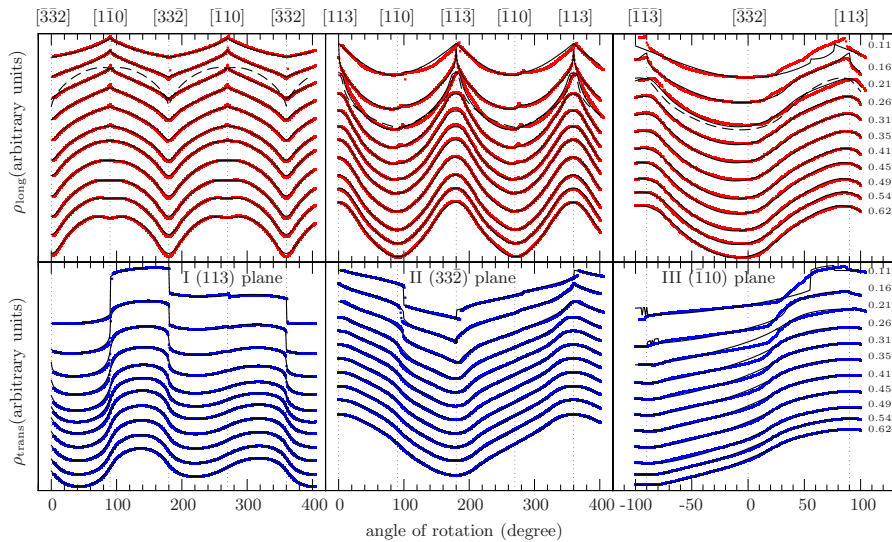


FIG. 7. (Color online) Angular dependence of the longitudinal and transverse resistivities at various external magnetic field strengths rotated within three different planes, referred to as configurations (I), (II), and (III), respectively (cf. Fig. 6). The sample contains nominally 4.9% Mn and the hydrostatical strain is $\varepsilon_h = -0.26\%$. The longitudinal-resistivity curves can be simulated using H -dependent resistivity parameters, cf. Fig. 8. In particular, for configuration (I) the longitudinal-resistivity parameters strongly vary with the field strength H . For comparison, simulated curves with the unchanged resistivity parameters as obtained at $\mu_0 H = 0.62$ T are shown for $\mu_0 H = 0.21$ T (dashed lines). The transverse-resistivity parameters are found to be constant within the experimental magnetic field range.

TABLE II. Anisotropy parameters of the samples under study as obtained from angle-dependent magnetotransport measurements.

x_{Mn} (%)	B_{x^4} (mT)	B_{z^4} (mT)	B_{z^2} (mT)	B_d (mT)	B_u (mT)
4.9	-46	-11	20	18	-8
4.2	-56	-25	20	12	-8
3.1	-65	-40	5	5	-5

plained by MA. A satisfactory agreement between theory and experiment can only be obtained by allowing for field-dependent longitudinal-resistivity parameters. In Fig. 8, the best-fit longitudinal-resistivity parameters of the sample with 4.9% Mn are plotted as a function of the magnetic field. The longitudinal-resistivity parameters of the samples with 4.2% and 3.1% Mn showed a similar field dependence. In contrast, the transverse resistivities shown in Fig. 7 can be simulated with field-independent resistivity parameters ρ_6 - ρ_{17} . In order to obtain a good fit of the experimental data, all parameters in Eq. (31) with exception of ρ_9 and ρ_{17} are required. The variation in the line shapes upon the field strength exclusively arises from the MA described by the anisotropy parameters from Eq. (21). Therefore, we mainly focused on the transverse resistivities when deriving MA parameters. Field-dependent resistivity parameters have also been reported by other groups for (113)A-oriented (Ga,Mn)As (Ref. 19) and for (001)-oriented (Ga,Mn)As.³⁷ In Ref. 37 the field dependence was studied up to 9 T.

The microscopic origin of these findings is not clear yet. A (001)-oriented reference sample, grown at the same conditions as the (113)A-oriented layer with $x_{\text{Mn}}=4.9\%$, showed a similar field dependence of the longitudinal resistivities, indicating that the effect is not primarily related to the substrate orientation.

IV. SUMMARY

Starting from a continuum mechanical treatment of the lattice distortion in high-index epilayers, a general expression for the strain tensor $\bar{\epsilon}$ of (*hhl*)-oriented layers was de-

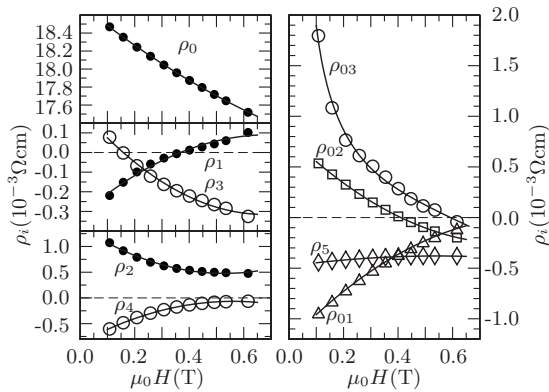


FIG. 8. Dependence of the longitudinal-resistivity parameters ρ_0 - ρ_{03} on the field strength $\mu_0 H$ for a (Ga,Mn)As(113)A layer with a manganese concentration of 4.9%. The decrease in ρ_0 with increasing $\mu_0 H$ reflects the negative magnetoresistance. The lines are guides to the eye.

rived. The isotropic strain component ϵ_h (and thus $\bar{\epsilon}$) as well as the shear angle ϕ were related to the experimentally accessible quantities $\Delta d/d$ and $\Delta\tau$. Applying the equations to the special case of (113)A orientation, ϵ_h and ϕ could be experimentally determined for a series of (113)A-oriented (Ga,Mn)As layers using HRXRD. Based on symmetry considerations, analytical expressions for the free-energy density and the resistivity tensor were derived by means of series expansions in terms of the magnetization components up to the fourth order, allowing for a phenomenological description of the MA and AMR, respectively. The anisotropy parameters were explicitly given as a function of the strain-tensor components. The expression for the resistivity tensor, deduced for monoclinic and orthorhombic crystal symmetries, can be used to calculate the longitudinal and transverse resistivities for arbitrary current directions. In order to probe the MA and AMR of the (Ga,Mn)As samples by angle-dependent magnetotransport, expressions for the resistivities were derived for current direction along $[33\bar{2}]$. The measurements were performed at 4.2 K and revealed the presence of a strong uniaxial anisotropy $B_{z^2}m_z^2$ along $[001]$ which could be explained within our theoretical model by the explicit form of $\bar{\epsilon}$. Further significant contributions to the MA were found to be $B_{z^4}m_z^4$, $B_{x^4}(m_x^4+m_y^4)$, $B_d(\mathbf{m}\cdot\mathbf{n})^2$, and $B_u(\mathbf{m}\cdot\mathbf{t})^2$. Whereas the transverse-resistivity parameters turned out to be nearly constant within the range of applied magnetic fields, the longitudinal-resistivity parameters were found to strongly depend on the field strength.

ACKNOWLEDGMENT

This work was supported by the Deutsche Forschungsgemeinschaft under Contract No. Li 988/4.

APPENDIX A: PARTIALLY RELAXED LAYERS

In this appendix, we describe how the equations presented in Sec. II A can be used to characterize partially relaxed layers. Figure 9 illustrates that the layer in the partially relaxed state can be described as a layer which is commensurate with a virtual cubic substrate having a lattice constant a_v . The hydrostatic strain in the layer is then described by the parameter

$$\epsilon_h^* = \frac{a_v - a_1}{a_1}, \quad (\text{A1})$$

where a_1 is the relaxed lattice parameter of the layer. In order to describe partially relaxed layers, we have to replace ϵ_h by

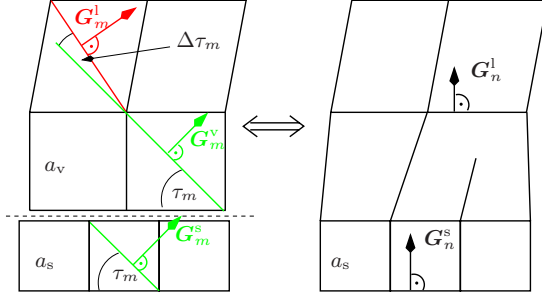


FIG. 9. (Color online) A partially relaxed layer can be thought of as a layer that pseudomorphically grows on a virtual cubic substrate with a lattice constant a_v different from the true substrate lattice constant a_s . Lattice planes m are parallel in real and virtual substrates. The relative inclination $\Delta\tau_m$ of the plane m in the layer with respect to m in the virtual substrate is the same as the inclination with respect to m in the real substrate. If the layer was tilted with respect to the substrate the reciprocal-lattice vectors \mathbf{G}_m^s and \mathbf{G}_n^l of a symmetric reflection would not be parallel. Note that in this schematic the cubes do not necessarily represent the cubic unit cells.

ε_h^* in all equations of Sec. II A. In particular, we obtain

$$\left(\frac{\Delta d}{d}\right)_m = \frac{d_m^l - d_m^v}{d_m^v} = \frac{\mathbf{m} \cdot \mathbf{a}(\varepsilon_h^*)}{1 + \varepsilon_h^*} \cos \tau_m, \quad (\text{A2})$$

$$\Delta\tau_m = \frac{\mathbf{m} \cdot \mathbf{a}(\varepsilon_h^*)}{1 + \varepsilon_h^*} \sin \tau_m \quad (\text{A3})$$

instead of Eqs. (5) and (6).

From a RSM around an asymmetric reflex ($m \neq n$), $\Delta\tau_m$ can be inferred because it is the angle between the reciprocal-lattice vector of layer \mathbf{G}_m^l and substrate \mathbf{G}_m^s , respectively, cf. Fig. 9. ε_h^* can then be obtained from Eq. (A3). Assuming that the lattice parameter of the (real) substrate is known, the reciprocal lattice of the substrate can serve as a reference; this allows an accurate measurement relative to the substrate without relying on the absolute angle scale of the diffractometer. The length of the layer's reciprocal-lattice vector $|\mathbf{G}_m^l|$ can be inferred from the RSM and consequently the lattice plane spacing of the layer $d_m^l = 2\pi/|\mathbf{G}_m^l|$ is obtained. By inserting ε_h^* into Eq. (A2), we find the value of d_m^v . Because the virtual substrate is cubic, we obtain $a_v = d_m^v \sqrt{h^2 + k^2 + l^2}$ and with Eq. (A1) we find a_1 . Thus we can determine the degree of relaxation

$$R = \frac{a_v - a_s}{a_1 - a_s}. \quad (\text{A4})$$

If the relaxed layer is tilted with respect to the substrate, as it has been reported for relaxed (In,Ga)As layers grown on (001)GaAs,⁴ this tilt needs to be considered in the determination of ε_h^* . The tilt angle $\psi = \angle(\mathbf{G}_n^l, \mathbf{G}_n^s)$ can be inferred from a RSM around a symmetric reflection ($m=n$) and the corrected angle $\Delta\tau_m^{\text{corr}} = \Delta\tau_m - \psi$ has to be inserted into Eq. (6) in order to obtain ε_h^* .

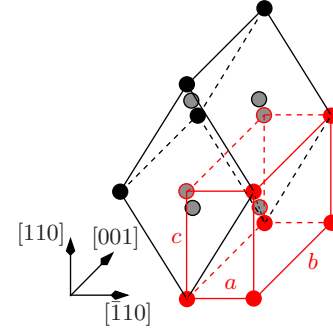


FIG. 10. (Color online) Distortion of the fcc cubic unit cell (black lines) when a layer with relaxed lattice constant a_1 is grown on a (110) plane of a substrate with lattice constant $a_s < a_1$. The gray points denote the face-centered atoms. For the zinc-blende lattice the only symmetry elements are a twofold rotational axis around [001] and two σ_v planes; thus the point group is $mm2$ (C_{2v}). The crystallographic unit cell of the body-centered orthorhombic Bravais lattice has the lattice parameters a , b , and c . Assuming pseudomorphic growth, the relations between the orthorhombic lattice parameters and the cubic lattice constant of the substrate are $a = a_s\sqrt{2}/2$ and $b = a_s$.

APPENDIX B: RESISTIVITY TENSOR FOR MONOCLINIC AND ORTHORHOMBIC SYMMETRIES

We derived the resistivity tensors for monoclinic and orthorhombic symmetries up to the fourth order in \mathbf{m} ; thereby we made use of von Neumann's principle as described in Ref. 31. In Fig. 10, we show that for (110)-oriented substrates the layer exhibits orthorhombic symmetry. For this case the generating matrices are

$$\bar{S}_3 = \begin{pmatrix} -1 & 0 & 0 \\ 0 & -1 & 0 \\ 0 & 0 & 1 \end{pmatrix} \quad (\text{B1})$$

and

$$\bar{S}_5 = \begin{pmatrix} 0 & 1 & 0 \\ 1 & 0 & 0 \\ 0 & 0 & 1 \end{pmatrix}. \quad (\text{B2})$$

Note that here the matrix \bar{S}_5 has been adapted to the cubic frame of reference, where the symmetry operation is a reflection at the xy plane and not a reflection at the y plane as in the canonical representation for the matrix \bar{S}_5 . We obtain for the resistivity tensor

$$\bar{\rho}_{\text{orthorhombic}} = \bar{\rho}_{\text{tetragonal}} + \Delta\bar{\rho}_{\text{orthorhombic}}, \quad (\text{B3})$$

where $\bar{\rho}_{\text{tetragonal}}$ is given by Eqs. (3)–(5) in Ref. 31 and $\Delta\bar{\rho}_{\text{orthorhombic}}$ by Eq. (B5), respectively.

For monoclinic symmetry, the only generating matrix is \bar{S}_5 and we find

$$\bar{\rho}_{\text{monoclinic}} = \bar{\rho}_{\text{orthorhombic}} + \Delta\bar{\rho}_{\text{monoclinic}}, \quad (\text{B4})$$

where $\Delta\bar{\rho}_{\text{monoclinic}}$ is given by Eq. (B6). The Greek letters in Eqs. (B5) and (B6) are nonvanishing linear combinations of the galvanomagnetic tensors, cf. Eq. (2) in Ref. 31,

$$\begin{aligned}
\Delta\bar{\rho}_{\text{orthorhombic}} = & \begin{pmatrix} 0 & \alpha_1 & 0 \\ \alpha_1 & 0 & 0 \\ 0 & 0 & 0 \end{pmatrix} + \begin{pmatrix} 0 & 0 & \beta_1 m_x \\ 0 & 0 & -\beta_1 m_y \\ -\beta_1 m_x & \beta_1 m_y & 0 \end{pmatrix} + \begin{pmatrix} 0 & \gamma_1(m_x^2 + m_y^2) & 0 \\ \gamma_1(m_x^2 + m_y^2) & 0 & 0 \\ 0 & 0 & 0 \end{pmatrix} + \begin{pmatrix} \gamma_2 m_x m_y & 0 & \gamma_4 m_y m_z \\ 0 & \gamma_2 m_x m_y & \gamma_4 m_x m_z \\ \gamma_4 m_y m_z & \gamma_4 m_x m_z & \gamma_3 m_x m_y \end{pmatrix} \\
& + \begin{pmatrix} 0 & 0 & \delta_1 m_x^3 \\ 0 & 0 & -\delta_1 m_y^3 \\ -\delta_1 m_x^3 & \delta_1 m_y^3 & 0 \end{pmatrix} + \begin{pmatrix} 0 & \delta_2 m_x m_y m_z & 0 \\ -\delta_2 m_x m_y m_z & 0 & 0 \\ 0 & 0 & 0 \end{pmatrix} + \begin{pmatrix} 0 & 0 & \delta_3 m_x m_y^2 \\ 0 & 0 & -\delta_3 m_x^2 m_y \\ -\delta_3 m_x m_y^2 & \delta_3 m_x^2 m_y & 0 \end{pmatrix} \\
& + \begin{pmatrix} 0 & \epsilon_1(m_x^4 + m_y^4) & 0 \\ \epsilon_1(m_x^4 + m_y^4) & 0 & 0 \\ 0 & 0 & 0 \end{pmatrix} + \begin{pmatrix} 0 & \epsilon_2 m_x^2 m_y^2 & 0 \\ \epsilon_2 m_x^2 m_y^2 & 0 & 0 \\ 0 & 0 & 0 \end{pmatrix} \\
& + \begin{pmatrix} \epsilon_3 m_x^3 m_y + \epsilon_4 m_x m_y^3 & 0 & \epsilon_5 m_x^3 m_z \\ 0 & \epsilon_3 m_x m_y^3 + \epsilon_4 m_x^3 m_y & \epsilon_5 m_x^3 m_z \\ \epsilon_5 m_x^3 m_z & \epsilon_5 m_x^3 m_z & \epsilon_6 m_x m_y(m_x^2 + m_y^2) \end{pmatrix} + \begin{pmatrix} 0 & 0 & \epsilon_7 m_x^2 m_y m_z \\ 0 & 0 & \epsilon_7 m_x m_y^2 m_z \\ \epsilon_7 m_x^2 m_y m_z & \epsilon_7 m_x m_y^2 m_z & 0 \end{pmatrix}, \quad (\text{B5})
\end{aligned}$$

$$\begin{aligned}
\Delta\bar{\rho}_{\text{monoclinic}} = & \begin{pmatrix} 0 & 0 & \alpha_2 \\ 0 & 0 & \alpha_2 \\ \alpha_2 & \alpha_2 & 0 \end{pmatrix} + \begin{pmatrix} 0 & \beta_2(m_x + m_y) & \beta_3 m_z \\ -\beta_2(m_x + m_y) & 0 & -\beta_3 m_z \\ -\beta_3 m_z & \beta_3 m_z & 0 \end{pmatrix} + \begin{pmatrix} 0 & 0 & \gamma_5 m_x^2 + \gamma_6 m_y^2 \\ 0 & 0 & \gamma_5 m_y^2 + \gamma_6 m_x^2 \\ \gamma_5 m_x^2 + \gamma_6 m_y^2 & \gamma_5 m_y^2 + \gamma_6 m_x^2 & 0 \end{pmatrix} \\
& + \begin{pmatrix} \gamma_8 m_x m_z + \gamma_9 m_y m_z & \gamma_{10} m_z(m_x + m_y) & \gamma_7 m_x m_y \\ \gamma_{10} m_z(m_x + m_y) & \gamma_8 m_y m_z + \gamma_9 m_x m_z & \gamma_7 m_x m_y \\ \gamma_7 m_x m_y & \gamma_7 m_x m_y & \gamma_{11} m_z(m_x + m_y) \end{pmatrix} + \begin{pmatrix} 0 & \delta_4(m_x^3 + m_y^3) & 0 \\ -\delta_4(m_x^3 + m_y^3) & 0 & 0 \\ 0 & 0 & 0 \end{pmatrix} \\
& + \begin{pmatrix} 0 & 0 & \delta_5 m_x m_y m_z \\ 0 & 0 & -\delta_5 m_x m_y m_z \\ -\delta_5 m_x m_y m_z & \delta_5 m_x m_y m_z & 0 \end{pmatrix} + \begin{pmatrix} 0 & \delta_8(m_x^2 m_y + m_x m_y^2) & \delta_6 m_x^2 m_z + \delta_7 m_y^2 m_z \\ -\delta_8(m_x^2 m_y + m_x m_y^2) & 0 & -\delta_6 m_y^2 m_z - \delta_7 m_x^2 m_z \\ -\delta_6 m_x^2 m_z - \delta_7 m_y^2 m_z & \delta_6 m_y^2 m_z + \delta_7 m_x^2 m_z & 0 \end{pmatrix} \\
& + \begin{pmatrix} 0 & 0 & \epsilon_8 m_x^4 + \epsilon_9 m_y^4 \\ 0 & 0 & \epsilon_8 m_y^4 + \epsilon_9 m_x^4 \\ \epsilon_8 m_x^4 + \epsilon_9 m_y^4 & \epsilon_8 m_y^4 + \epsilon_9 m_x^4 & 0 \end{pmatrix} + \begin{pmatrix} 0 & 0 & \epsilon_{10} m_x^2 m_y^2 \\ 0 & 0 & \epsilon_{10} m_x^2 m_y^2 \\ \epsilon_{10} m_x^2 m_y^2 & \epsilon_{10} m_x^2 m_y^2 & 0 \end{pmatrix} \\
& + \begin{pmatrix} \epsilon_{11} m_x^3 m_z + \epsilon_{12} m_y^3 m_z & \epsilon_{15} m_z(m_x^3 + m_y^3) & \epsilon_{13} m_x^3 m_y + \epsilon_{14} m_x m_y^3 \\ \epsilon_{15} m_z(m_x^3 + m_y^3) & \epsilon_{11} m_y^3 m_z + \epsilon_{12} m_x^3 m_z & \epsilon_{13} m_x m_y^3 + \epsilon_{14} m_x^3 m_y \\ \epsilon_{13} m_x^3 m_y + \epsilon_{14} m_x m_y^3 & \epsilon_{13} m_x m_y^3 + \epsilon_{14} m_x^3 m_y & \epsilon_{16} m_z(m_x^3 + m_y^3) \end{pmatrix} \\
& + \begin{pmatrix} \epsilon_{17} m_x^2 m_y m_z + \epsilon_{18} m_x m_y^2 m_z & \epsilon_{19} m_x m_y m_z(m_x + m_y) & 0 \\ \epsilon_{19} m_x m_y m_z(m_x + m_y) & \epsilon_{17} m_x m_y^2 m_z + \epsilon_{18} m_x^2 m_y m_z & 0 \\ 0 & 0 & \epsilon_{20} m_x m_y m_z(m_x + m_y) \end{pmatrix}. \quad (\text{B6})
\end{aligned}$$

*Present address: Walter Schottky Institut, Technische Universität München, 85748 Garching, Germany; dreher@wsi.tum.de

¹T. Dietl, H. Ohno, and F. Matsukura, *Phys. Rev. B* **63**, 195205 (2001).

²T. Jungwirth, J. Sinova, J. Masek, J. Kucera, and A. H. MacDonald, *Rev. Mod. Phys.* **78**, 809 (2006).

³V. Novák, K. Olejnik, J. Wunderlich, M. Cukr, K. Vyborny, A. W. Rushforth, K. W. Edmonds, R. P. Campion, B. L. Gallagher, J. Sinova, and T. Jungwirth, *Phys. Rev. Lett.* **101**, 077201 (2008).

⁴M. Glunk, J. Daubler, L. Dreher, S. Schwaiger, W. Schoch, R. Sauer, W. Limmer, A. Brandmaier, S. T. B. Goennenwein, C. Bihler, and M. S. Brandt, *Phys. Rev. B* **79**, 195206 (2009).

⁵J. Zemen, J. Kucera, K. Olejnik, and T. Jungwirth, *Phys. Rev. B* **80**, 155203 (2009).

⁶E. De Ranieri, A. W. Rushforth, K. Vyborny, U. Rana, E. Ahmad, R. P. Campion, C. T. Foxon, B. L. Gallagher, A. C. Irvine, J. Wunderlich, and T. Jungwirth, *New J. Phys.* **10**, 065003 (2008).

⁷A. W. Rushforth, K. Vyborny, C. S. King, K. W. Edmonds, R. P.

- Campion, C. T. Foxon, J. Wunderlich, A. C. Irvine, P. Vasek, V. Novak, K. Olejnik, J. Sinova, T. Jungwirth, and B. L. Gallagher, *Phys. Rev. Lett.* **99**, 147207 (2007).
- ⁸A. Rushforth, K. Vyborny, C. King, K. Edmonds, R. Campion, C. Foxon, J. Wunderlich, A. Irvine, V. Novak, K. Olejnik, A. Kovalev, J. Sinova, T. Jungwirth, and B. Gallagher, *J. Magn. Mater.* **321**, 1001 (2009).
- ⁹C. Bihler, M. Althammer, A. Brandlmaier, S. Geprägs, M. Weiler, M. Opel, W. Schoch, W. Limmer, R. Gross, M. S. Brandt, and S. T. B. Goennenwein, *Phys. Rev. B* **78**, 045203 (2008).
- ¹⁰M. Overby, A. Chernyshov, L. P. Rokhinson, X. Liu, and J. K. Furdyna, *Appl. Phys. Lett.* **92**, 192501 (2008).
- ¹¹S. T. B. Goennenwein, M. Althammer, C. Bihler, A. Brandlmaier, S. Geprägs, M. Opel, W. Schoch, W. Limmer, R. Gross, and M. S. Brandt, *Phys. Status Solidi (RRL)* **2**, 96 (2008).
- ¹²A. W. Rushforth, E. De Ranieri, J. Zemen, J. Wunderlich, K. W. Edmonds, C. S. King, E. Ahmad, R. P. Campion, C. T. Foxon, B. L. Gallagher, K. Vyborny, J. Kucera, and T. Jungwirth, *Phys. Rev. B* **78**, 085314 (2008).
- ¹³J. Wenisch, C. Gould, L. Ebel, J. Storz, K. Pappert, M. J. Schmidt, C. Kumpf, G. Schmidt, K. Brunner, and L. W. Molenkamp, *Phys. Rev. Lett.* **99**, 077201 (2007).
- ¹⁴J. Wunderlich, A. C. Irvine, J. Zemen, V. Holy, A. W. Rushforth, E. De Ranieri, U. Rana, K. Vyborny, J. Sinova, C. T. Foxon, R. P. Campion, D. A. Williams, B. L. Gallagher, and T. Jungwirth, *Phys. Rev. B* **76**, 054424 (2007).
- ¹⁵T. Omiya, F. Matsukura, A. Shen, Y. Ohno, and H. Ohno, *Physica E* **10**, 206 (2001).
- ¹⁶K. Y. Wang, K. W. Edmonds, L. X. Zhao, M. Sawicki, R. P. Campion, B. L. Gallagher, and C. T. Foxon, *Phys. Rev. B* **72**, 115207 (2005).
- ¹⁷C. Bihler, H. Huebl, M. S. Brandt, S. T. B. Goennenwein, M. Reinwald, U. Wurstbauer, M. Doppe, D. Weiss, and W. Wegscheider, *Appl. Phys. Lett.* **89**, 012507 (2006).
- ¹⁸W. Limmer, M. Glunk, J. Daeubler, T. Hummel, W. Schoch, R. Sauer, C. Bihler, H. Huebl, M. S. Brandt, and S. T. B. Goennenwein, *Phys. Rev. B* **74**, 205205 (2006).
- ¹⁹M. T. Elm, P. J. Klar, W. Heimbrod, U. Wurstbauer, M. Reinwald, and W. Wegscheider, *J. Appl. Phys.* **103**, 093710 (2008).
- ²⁰W. Limmer, J. Daeubler, M. Glunk, T. Hummel, W. Schoch, and R. Sauer, *Microelectron. J.* **37**, 1535 (2006).
- ²¹J. Hornstra and W. J. Bartels, *J. Cryst. Growth* **44**, 513 (1978).
- ²²C. R. Wie, *J. Appl. Phys.* **66**, 985 (1989).
- ²³Ioffe Institute, *Physical properties of semiconductors* <http://www.ioffe.ru/SVA/NSM/> (consulted in December 2008).
- ²⁴W. J. Bartels and W. Nijman, *J. Cryst. Growth* **44**, 518 (1978).
- ²⁵U. Welp, V. K. Vlasko-Vlasov, X. Liu, J. K. Furdyna, and T. Wojtowicz, *Phys. Rev. Lett.* **90**, 167206 (2003).
- ²⁶M. Sawicki, K.-Y. Wang, K. W. Edmonds, R. P. Campion, C. R. Staddon, N. R. S. Farley, C. T. Foxon, E. Papis, E. Kaminska, A. Piotrowska, T. Dietl, and B. L. Gallagher, *Phys. Rev. B* **71**, 121302(R) (2005).
- ²⁷K. Hamaya, T. Taniyama, Y. Kitamoto, T. Fujii, and Y. Yamazaki, *Phys. Rev. Lett.* **94**, 147203 (2005).
- ²⁸K. Hamaya, T. Watanabe, T. Taniyama, A. Oiwa, Y. Kitamoto, and Y. Yamazaki, *Phys. Rev. B* **74**, 045201 (2006).
- ²⁹S. V. Vonsowskii, *Magnetism* (Wiley, New York, 1974), Vol. II.
- ³⁰In Refs. 4 and 31, these parameters were labeled $B_{2\perp}$, $B_{4\parallel}$, and $B_{4\perp}$, respectively.
- ³¹W. Limmer, J. Daeubler, L. Dreher, M. Glunk, W. Schoch, S. Schwaiger, and R. Sauer, *Phys. Rev. B* **77**, 205210 (2008).
- ³²W. Limmer, A. Koeder, S. Frank, V. Avrutin, W. Schoch, R. Sauer, K. Zuern, J. Eisenmenger, P. Ziemann, E. Peiner, and A. Waag, *Phys. Rev. B* **71**, 205213 (2005).
- ³³J. Daeubler, M. Glunk, W. Schoch, W. Limmer, and R. Sauer, *Appl. Phys. Lett.* **88**, 051904 (2006).
- ³⁴W. T. Stacy and M. M. Janssen, *J. Cryst. Growth* **27**, 282 (1974).
- ³⁵G. Bauer and W. Richter, *Optical Characterization of Epitaxial Semiconductor Layers* (Springer-Verlag Telos, Berlin, 1996).
- ³⁶M. Glunk, J. Daeubler, W. Schoch, R. Sauer, and W. Limmer, *Phys. Rev. B* **80**, 125204 (2009).
- ³⁷D. Wu, P. Wei, E. Johnston-Halperin, D. D. Awschalom, and J. Shi, *Phys. Rev. B* **77**, 125320 (2008).